



Dealloying behavior of amorphous binary Ti–Cu alloys in hydrofluoric acid solutions at various temperatures



Zhenhua Dan^{a,b,*}, Fengxiang Qin^a, Shin-ichi Yamaura^a, Yu Sugawara^b, Izumi Muto^b, Nobuyoshi Hara^b

^a Institute for Materials Research, Tohoku University, Sendai 9808577, Japan

^b Department of Materials Science, Tohoku University, Sendai 9808579, Japan

ARTICLE INFO

Article history:

Received 1 February 2013

Received in revised form 27 May 2013

Accepted 21 July 2013

Available online 30 July 2013

Keywords:

Amorphous materials

Nanostructured materials

Corrosion

Diffusion

Transmission electron microscopy

ABSTRACT

A nanoporous copper structure was fabricated from amorphous binary Ti_xCu_{100-x} ($x = 40, 50$ and 60 at.%) alloys in hydrofluoric acid solutions under a free corrosion condition. A bi-continuous nanoporous structure has a pore size of 25–75 nm and a ligament size of 46–79 nm in 0.03 M HF solution. In 0.13 M HF solution, a pore size of 85–380 nm and a ligament size of 80–338 nm were obtained. The dealloying process is thermal-activated and obeys the Arrhenius law. The surface diffusivity decreases with temperature and concentrations of dealloying solutions. The values of the activation energy of copper adatoms are estimated to be 40.3–78.1 kJ mol⁻¹, which depend not only on the alloy composition but also on the dealloying electrolyte composition.

© 2013 Elsevier B.V. All rights reserved.

1. Introduction

Nanoporous metals have attracted much attention due to their potential in various applications, but especially as catalyst, sensors, and actuators [1–4]. Nanoporous silver, gold, platinum were fabricated from a dealloying process by many research groups [5–8]. Monolithic nanoporous copper (NPC) was fabricated from abundant crystalline alloy systems, for instance, Al–Cu [5] and Mn–Cu [9,10]. Recently, the NPC was fabricated by dealloying amorphous Ti–Cu alloys in hydrofluoric acids [11]. From an electrochemical perspective, the standard electrode potentials of Ti and Cu (–1.630 V vs. the standard hydrogen electrode (SHE) for Ti/Ti²⁺ and 0.342 V vs. SHE for Cu/Cu²⁺) differ as much as 1.972 V [12], which promise selective leaching of Ti from binary Ti–Cu alloys in an appropriate HF solution, where Ti dissolves as stable ions such as TiF₆²⁻. The uniform nanoporous structure was fabricated more readily from the amorphous alloys because amorphous alloys can be characterized by their disordered atomic-scale structure and an absence of defects and heterogeneous microstructures, i.e. grain boundaries, second phases and element segregation [13,14].

The evolution of the nanoporosity is regarded as a spinodal decomposition process, and the dealloying is dynamically evoked

at the solid/electrolyte interface. Moreover, the dealloying, as a thermally-activated process, obeys the Arrhenius relationship [7,8,15–17]. The evolution of nanoporosity might be affected by material factors (the composition in the alloy systems; the crystalline properties), the dealloying temperatures and dealloying electrolytes. The activation energy for the coarsening of NPC during dealloying process has been reported to be 47.7 and 145.3 kJ mol⁻¹ in HCl solutions, which corresponds to NPCs with different pore sizes formed in various regions where the phase separation occurs during dealloying in the crystalline Al–Cu alloy systems [15]. The surface diffusivity exhibits a dependency on the reciprocal of temperature, and well obeys the Arrhenius law. Qian et al. [7] investigated the dealloying behavior of binary Ag₆₅Au₃₅ alloy in concentrated HNO₃ solution at temperatures of –25, 0, and 25 °C, and they found that the coarsening rates and surface relaxing depend on temperature and etching time. However, the dependency of the NPC formation on amorphous Ti–Cu precursors in HF solutions is still remaining unclear.

The present research focused on the dealloying behavior of amorphous Ti–Cu precursors in aspects of their electrochemical reactions and evolution of nanoporous structures. The starting materials, amorphous binary Ti_xCu_{100-x} ($x = 40, 50$ and 60 at.%) alloys, were immersed in HF solutions under a free corrosion condition at different dealloying temperatures. The characteristic scale length of the nanopores and ligaments of NPCs was investigated at different temperatures. The surface diffusivity and activation energy during the NPC formation was also investigated.

* Corresponding author. Address: Institute for Materials Research, Tohoku University 2-1-1, Katahira, Aoba-ku, Sendai 9808579, Japan. Tel.: +81 22 215 2718; fax: +81 22 215 2714.

E-mail address: zhenhuadan@imr.tohoku.ac.jp (Z. Dan).

2. Experimental procedure

Binary Ti–Cu alloys with nominal compositions of 40, 50, 60 at.% Cu were prepared by arc melting of the mixture of pure Ti (99.99 wt%) and pure Cu (99.9 wt%) in an Ar atmosphere. The melt spinning method was used to prepare Ti–Cu amorphous ribbons with 20 μm in thickness and 2 mm in width. The dealloying was performed in 0.03 M and 0.13 M HF solutions under a free corrosion condition open to air for 10.8 ks at temperatures of 298 K, 323 K and 348 K. The pH of 0.03 M and 0.13 M HF solution was 3.3 and 2.90, respectively. The amorphicity of the as-spun Ti–Cu samples and the dealloyed alloys was confirmed by XRD using an X-ray diffractometer (Rigaku, RINT 4200). The microstructures of dealloyed Ti–Cu ribbons were investigated by a transmission electron microscope (JEOL, JEM-HC2100) and a high-resolution transmission electron microscope (JEOL, JEM-ARM210F). The TEM sampling was conducted by an ion milling method. The morphology of the dealloyed samples was observed by a scanning electron microscope (JEOL, JIB-4610F) equipped with an energy dispersive X-ray spectroscopy (EDX).

3. Results

3.1. Characterization of microstructure of as-spun Ti–Cu alloys

The XRD patterns of as-spun and dealloyed Ti–Cu ribbons are showed in Fig. 1. A broad diffraction peak appeared in the XRD patterns of as-spun $\text{Ti}_{40}\text{Cu}_{60}$, $\text{Ti}_{50}\text{Cu}_{50}$ and $\text{Ti}_{60}\text{Cu}_{40}$ ribbons at an angle around 2θ of 41° , which is typical of the amorphous alloys. The amorphicity of Ti–Cu alloys remained at a wide range of Cu contents. The diffraction peaks of dealloyed ribbons were assigned to Cu (111), (200) and (220). The small peak at $2\theta = 36.6^\circ$ in Fig. 1a was risen from Cu_2O (111), and other diffraction peaks from

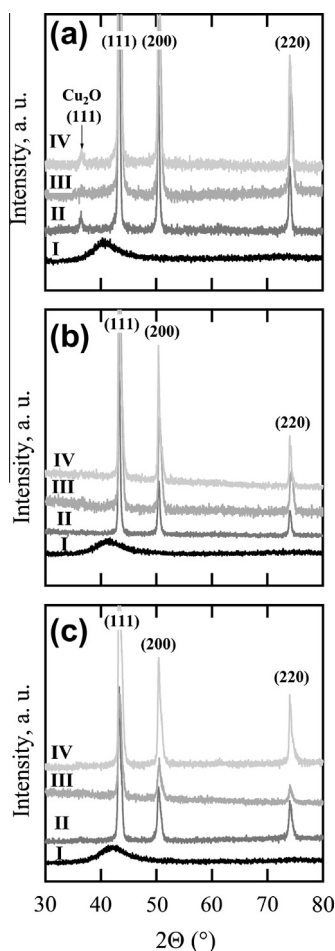


Fig. 1. XRD patterns of $\text{Ti}_{60}\text{Cu}_{40}$ (a), $\text{Ti}_{50}\text{Cu}_{50}$ (b) and $\text{Ti}_{40}\text{Cu}_{60}$ (c) amorphous ribbons before (I) and after dealloying in 0.13 M HF solution for 10.8 ks at different temperatures of 298 K (II), 323 K (III) and 348 K (IV).

Cu_2O overlapped with those from Cu. The formation of Cu_2O phases was confirmed on the residual porous Cu on dealloyed $\text{Ti}_{60}\text{Cu}_{40}$ ribbons. On the contrary, no visible Cu_2O peaks appeared on dealloyed $\text{Ti}_{50}\text{Cu}_{50}$ and $\text{Ti}_{40}\text{Cu}_{60}$ ribbons. Therefore, the residue of dealloyed alloys had the structure of face-centered cubic (fcc) Cu (JCPDS card No.: 02-1225) and trace Cu_2O (JCPDS card No.: 74-1230) in some cases. The fcc Cu residue was confirmed for all ribbons dealloyed at three different temperatures. Sherrer's equation [18] was used to estimate the grain size for $\text{Ti}_{60}\text{Cu}_{40}$, $\text{Ti}_{50}\text{Cu}_{50}$ and $\text{Ti}_{40}\text{Cu}_{60}$ ribbons after dealloying in 0.13 M HF solution at different temperatures. The values of the calculated grain size are listed in Table 1. The Cu grain sizes decreased with an increase in Cu contents in the precursors.

3.2. Morphology of dealloyed Ti–Cu alloys

Fig. 2 shows the surface morphology of dealloyed $\text{Ti}_{60}\text{Cu}_{40}$ and $\text{Ti}_{50}\text{Cu}_{50}$ ribbon alloys in 0.03 M and 0.13 M HF solutions at 298 K. The dealloyed ribbons exhibited an open, bi-continuous interpenetrating pore-to-ligament structure with length scales of few tenth nanometers to several hundredth nanometers. The cross-sectional morphology show that the NPCs had three-dimensional structures, and the NPC pore sizes decreased while Cu atomic ratios in the Ti–Cu ribbons increased. The figures which are shown below the SEM graphs indicate the distribution of pore and ligament sizes of NPCs. The pore sizes and ligament sizes were estimated by the single chord length method over 150 sites of SEM morphology. The mean values of nanopores of $\text{Ti}_{60}\text{Cu}_{40}$ and $\text{Ti}_{50}\text{Cu}_{50}$ ribbon alloys were found to be 37 nm and 31 nm in 0.03 M HF solution, and 86 nm and 185 nm in 0.13 M HF solution, respectively. The mean values of ligament sizes were confirmed to be 46 nm and 57 nm in 0.03 M HF solution, and 94 nm and 185 nm in 0.13 M HF solution, respectively. The nanoporous structures formed in dilute HF solutions had smaller pores and narrow ligaments, which indicated their higher nanoporosity. With an increase in Cu contents, the nanopores became smaller for $\text{Ti}_{60}\text{Cu}_{40}$ and $\text{Ti}_{40}\text{Cu}_{60}$ ribbon alloys.

Fig. 3 shows the nanoporous structures of dealloyed $\text{Ti}_{60}\text{Cu}_{40}$ and $\text{Ti}_{40}\text{Cu}_{60}$ ribbons after immersion of 10.8 ks at 323 K and 348 K. The nanopores formed on $\text{Ti}_{60}\text{Cu}_{40}$ ribbons at 323 K and 348 K had a characteristic pore size of 170 nm and 227 nm, and those of $\text{Ti}_{40}\text{Cu}_{60}$ ribbon samples were 121 nm and 246 nm, respectively. In general, it could be observed that the pore sizes increased with the dealloying temperature. The EDX spectra of dealloyed $\text{Ti}_{40}\text{Cu}_{60}$ ribbon alloy indicated that residue was Cu, and other elements, such as C and Re, were from the adhesive tapes and SEM electron guns. The residue consisted of trace Ti element, and Ti contents seemed slightly higher on the samples dealloyed at higher temperatures.

The changes in pore sizes and ligament sizes measured from SEM morphology are summarized in Fig. 4 as a function of dealloying temperature. The nanopores increase with increasing temperature as well as HF concentration except some cases for $\text{Ti}_{50}\text{Cu}_{50}$ and $\text{Ti}_{60}\text{Cu}_{40}$ samples. The nanopores formed on amorphous $\text{Ti}_{50}\text{Cu}_{50}$

Table 1

Cu grain sizes of NPCs obtained from amorphous ribbons after dealloying in 0.13 M HF solution for 10.8 ks at different temperatures. Grain sizes are calculated according to Scherrer equation [18] (unit: nm).

Alloys	Temperature		
	298 K	323 K	348 K
$\text{Ti}_{40}\text{Cu}_{60}$	24	19	25
$\text{Ti}_{50}\text{Cu}_{50}$	21	17	24
$\text{Ti}_{60}\text{Cu}_{40}$	16	14	19

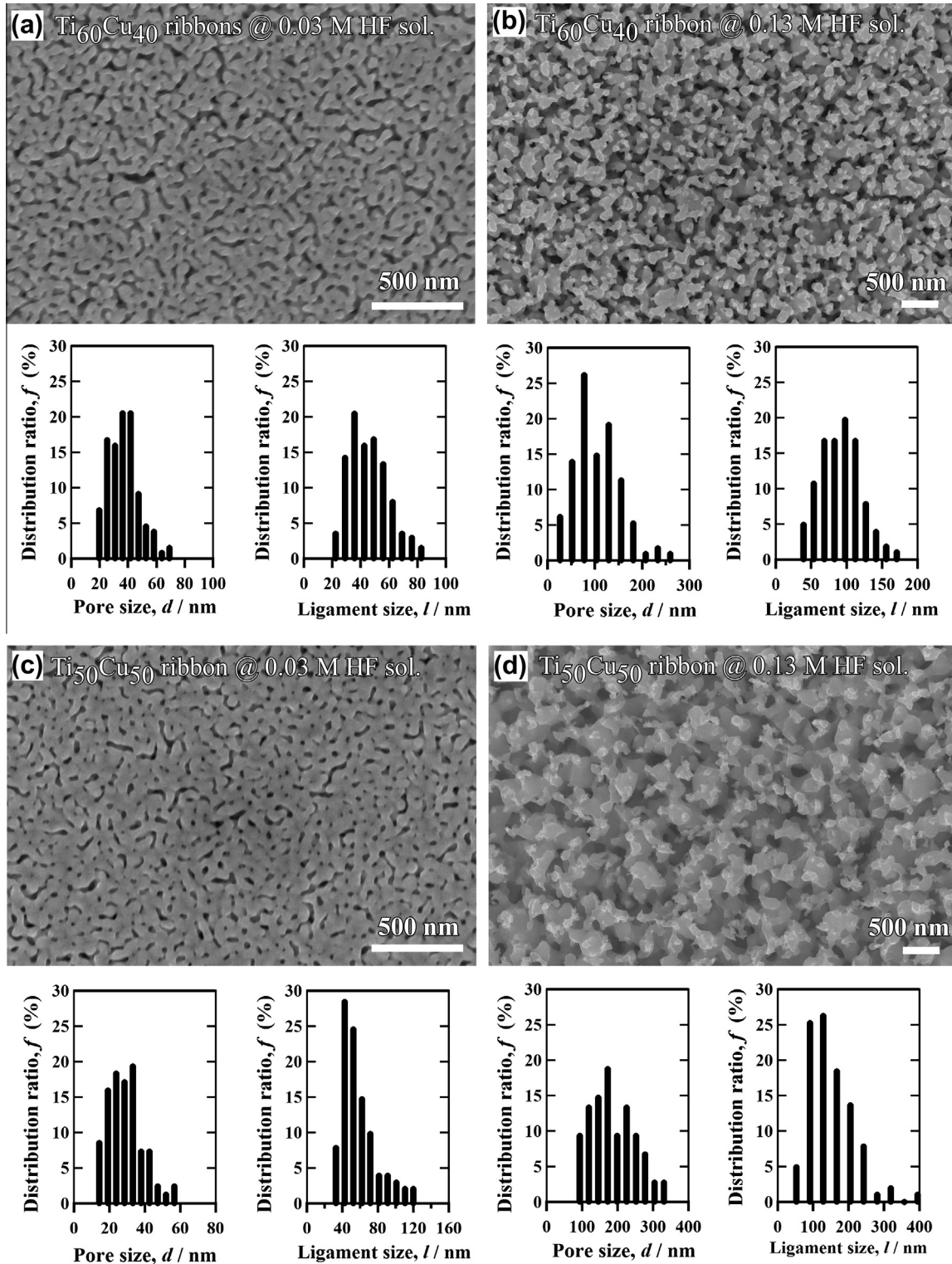


Fig. 2. SEM morphology of dealloyed $\text{Ti}_{60}\text{Cu}_{40}$ and $\text{Ti}_{50}\text{Cu}_{50}$ amorphous ribbons after dealloying in 0.03 M (a and c) and 0.13 M (b and d) HF solution for 10.8 ks at 298 K. The size distribution ratios of nanopores and ligaments are shown below the corresponding SEM morphology.

ribbon alloys in both 0.03 and 0.13 M HF solutions are relatively larger than those obtained on $\text{Ti}_{60}\text{Cu}_{40}$ and $\text{Ti}_{40}\text{Cu}_{60}$ ribbons.

3.3. Characteristics of dealloyed Ti–Cu alloys

Fig. 5a–c shows the bright-field TEM image, the high-resolution TEM (HR-TEM) image and selective area diffraction patterns (SAD

pattern) of dealloyed $\text{Ti}_{40}\text{Cu}_{60}$ ribbons immersed in 0.03 M HF solution at 348 K for 10.8 ks. The three-dimensional bi-continuous porous structure is clearly visible, and the characteristic pore size was confirmed to be 38 nm for the internal nanoporous structures. On the other hand, the characteristic pore size confirmed from SEM images was 68 nm, which indicated that the nanoporous structure formed in the internal regions had a finer structure. As shown in

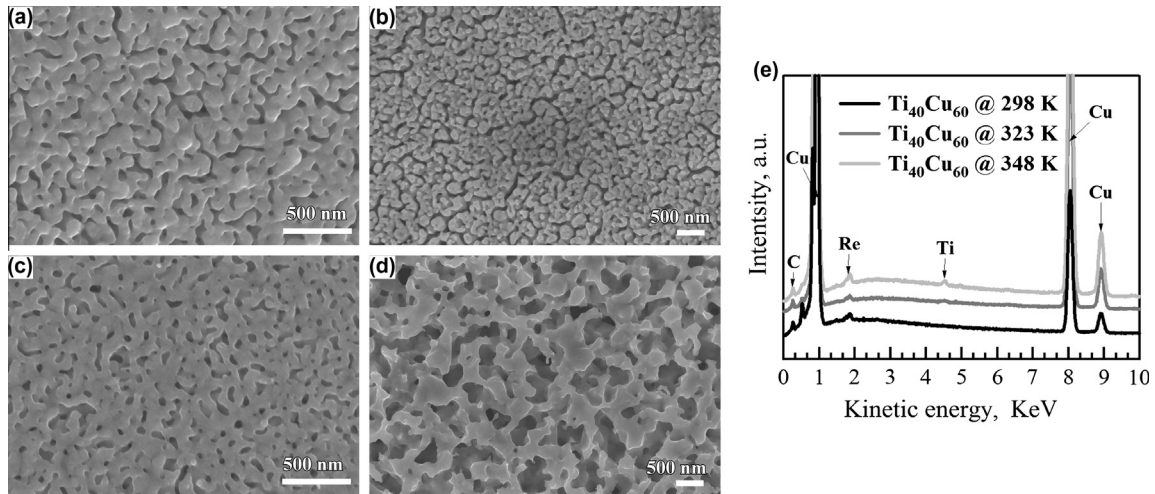


Fig. 3. SEM morphology of dealloyed $\text{Ti}_{60}\text{Cu}_{40}$ and $\text{Ti}_{40}\text{Cu}_{60}$ ribbons after dealloying in 0.13 M HF solution at 323 K (a and c) and 348 K (b and d) for 10.8 ks and the typical EDX spectra (e) of dealloyed $\text{Ti}_{40}\text{Cu}_{60}$ ribbons after dealloying in 0.13 M HF solution for 10.8 ks at different temperatures.

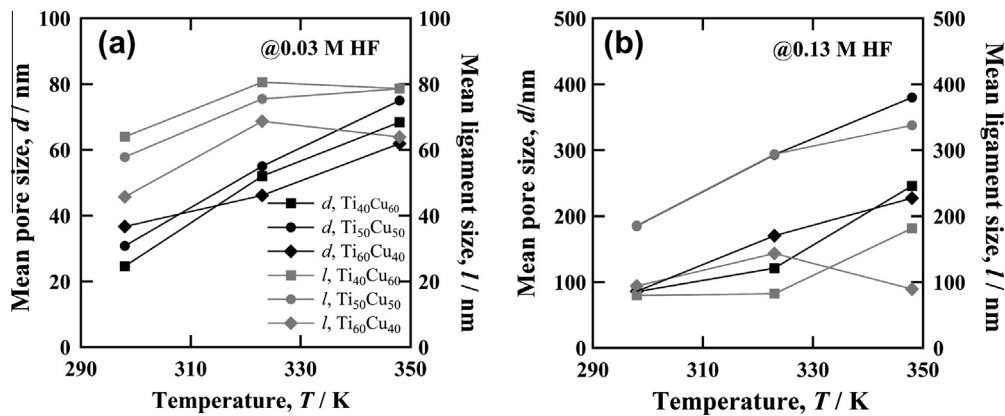


Fig. 4. The mean pore size, d , and mean ligament size, l , of dealloyed $\text{Ti}_{40}\text{Cu}_{60}$, $\text{Ti}_{50}\text{Cu}_{50}$ and $\text{Ti}_{60}\text{Cu}_{40}$ ribbon alloys as a function of temperature, T , in 0.03 M HF solution (a) and 0.13 M HF solution (b).

Fig. 5b, the interplanar distance from the adjacent lattice fringes marked in the HR-TEM images was 0.209 nm, corresponding to the {111} planes of *fcc* Cu. The lattice constants of residue Cu estimated from XRD analysis were found to have values of 0.3609–0.3619 nm, which are slightly larger than that of pure Cu of 0.3607 nm. The HR-TEM image shows that the NPCs have a polycrystalline structure, indicating the original Cu atoms are rearranged to form a crystalline structure as they were dealloyed [16,17]. As shown in Fig. 5c, the diffraction rings are assigned to Cu (111), (200), (220), (311) and (222). The Cu_2O specie was not detected in the TEM observation, which is consistent with XRD patterns (Fig. 1c). The SAD pattern indicated that the dealloyed $\text{Ti}_{40}\text{Cu}_{60}$ ribbons have the structure of *fcc* Cu.

3.4. Estimation of surface diffusivity

On the basis of the surface diffusion controlled coarsening mechanism, the surface diffusivity, D_s , at various dealloying temperature was estimated by the equation [19]:

$$D_s = \frac{[d(t)]^4 kT}{32\gamma t \alpha^4} \quad (1)$$

where k is Boltzmann constant ($1.3806 \times 10^{-23} \text{ J K}^{-1}$), γ is surface energy, t is the dealloying time (10 800 s), $d(t)$ is the pore size at t ,

T is the temperature, and α is the lattice constant. The surface energy is considered to be 1.79 J m^{-2} for Cu [7,19]. The lattice constants of NPCs obtained from the XRD data were used to calculate the surface diffusivity.

Since the dealloying process is considered to be a thermally-activated process, the measurement of the activation energy will be helpful for understanding the dealloying mechanisms. The Arrhenius equation used for describing for surface diffusion process is as follows [20]:

$$D_s = D_0 \exp\left(-\frac{E_a}{RT}\right) \quad (2)$$

where D_0 is the diffusion constant, R is the gas constant and E_a is the activation energy for the surface diffusion process.

The surface diffusivity of $\text{Ti}_{60}\text{Cu}_{40}$ ribbon alloy dealloyed in 0.03 M HF solution was estimated to be $7.08 \times 10^{-19} \text{ m}^2 \text{ s}^{-1}$ at 298 K and $6.66 \times 10^{-18} \text{ m}^2 \text{ s}^{-1}$ at 348 K. On the other hand, the surface diffusivity of $\text{Ti}_{60}\text{Cu}_{40}$ ribbon alloy dealloyed in 0.13 M HF solution was estimated to be $2.16 \times 10^{-17} \text{ m}^2 \text{ s}^{-1}$ at 298 K and $1.21 \times 10^{-15} \text{ m}^2 \text{ s}^{-1}$ at 348 K. The surface diffusivity increased almost one order of magnitude due to the increase in dealloying temperature, and the drastic increase in the surface diffusivity in the concentrated HF solutions was more than 2 orders of magnitude, which indicates that the effect of dealloying temperature on evolution of nanoporosity in concentrated HF solutions was

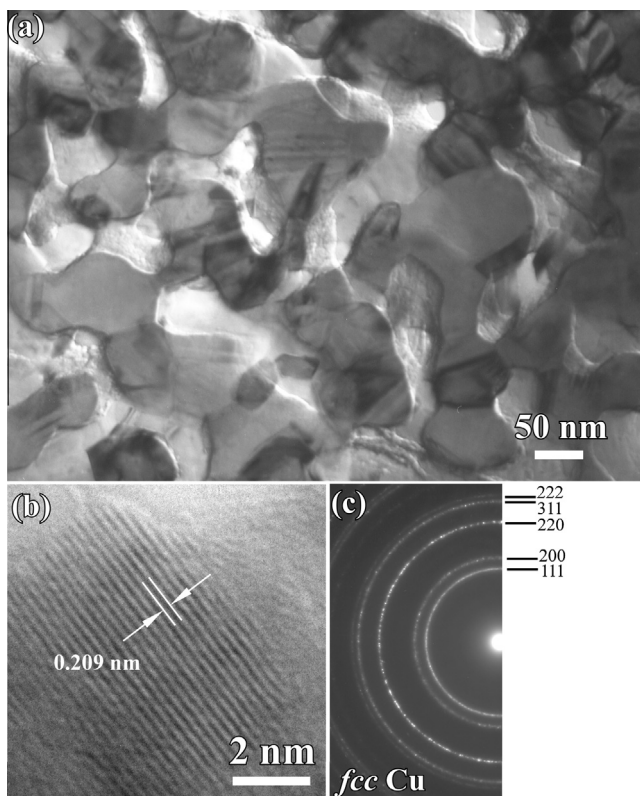


Fig. 5. Bright-field TEM image (a), HR-TEM image (b) and SAD pattern (c) of $\text{Ti}_{40}\text{Cu}_{60}$ ribbons dealloying in 0.03 M HF solution after dealloying for 10.8 ks at 348 K.

much stronger than that in diluted HF solutions. This fact revealed that the larger nanopores formed preferentially in the concentrated HF solution at the higher dealloying temperatures. The surface diffusivity at 348 K was estimated to be $2.30 \times 10^{-16} \text{ m}^2 \text{ s}^{-1}$ for $\text{Ti}_{40}\text{Cu}_{60}$ ribbon alloy and $9.45 \times 10^{-15} \text{ m}^2 \text{ s}^{-1}$ for $\text{Ti}_{50}\text{Cu}_{50}$ ribbon alloy in 0.13 M HF solution. The surface diffusivity of $\text{Ti}_{50}\text{Cu}_{50}$ ribbon alloys dealloyed in 0.13 M HF solution was larger than the other binary alloy systems, which in fact caused the severe surface relaxation and the formation of rough nanopores. Fig. 6 shows the Arrhenius plots of $\ln(D_s)$ vs. $1000/T$ of each Ti–Cu alloy in 0.03 M and 0.13 M HF solutions. Good linear relationships were obtained for the experimental data. The strong temperature dependence of the

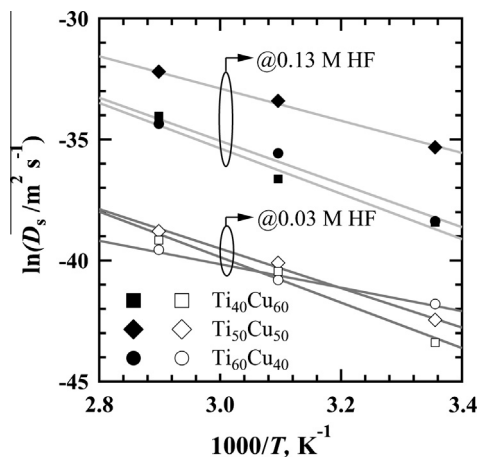


Fig. 6. Arrhenius plot of natural logarithm of surface diffusivity, $\ln(D_s)$, vs. the reciprocal of temperature, $1000/T$.

nanopore size and surface diffusivity presented here is consistent with the recent kinetic Monte Carlo simulation [17]. The value of activation energy and diffusion constants extracted from the slopes ($-E_a/R$) and the intercepts ($\ln D_0$) of Fig. 6 are listed in Table 2. The activation energy was found to have values in the range from 40.3 to 78.1 kJ mol^{-1} for Ti–Cu alloy systems. The activation energy is strongly depended on the alloy composites of the amorphous Ti–Cu precursors.

3.5. Discussion

The formation of NPCs during dealloying includes several steps: (1) The breakdown of native TiO_2 oxide layer. (2) The selective dissolution of Ti atoms. (3) The diffusion of Cu adatoms. (4) The rearrangements of Cu adatoms and the formation of ligaments.

From the perspectives of electrochemistry, the native TiO_2 layer with a thickness about 2–5 nm was broken down since the fluoride ions triggered the formation reactions of high soluble fluoride complex (i.e. TiF_6^{2-} , TiF_2^+) [21]. Meanwhile, the bare Ti substrates were attacked by F^- ions continuously, which is a selective dissolution process of Ti atoms from Ti–Cu matrix. Our former research results indicated that the dissolution of Ti elements was so fast in 0.13 M HF solution that the Cu contents in the surface regions became over 90 at.% for $\text{Ti}_{40}\text{Cu}_{60}$ alloy, over 97 at.% for $\text{Ti}_{50}\text{Cu}_{50}$ alloy and over 99 at.% for $\text{Ti}_{60}\text{Cu}_{40}$ alloy after the first immersion of 600 s. On the other hand, the change of Cu contents in 0.03 M HF solution was relatively slow [11]. The F^- ions had an ability to produce more active corrosion potential and to decrease the anodic and cathodic (hydrogen evolution) Tafel slopes, which resulted in the increase of dissolution rates of Ti atoms in the concentrated HF solutions. The critical corrosion currents of Ti electrodes in H_2SO_4 and NaF increased more than 3 orders of magnitude when the NaF concentration increased from 0 to 0.12 M [21]. The behavior described above is also enhanced by temperature. With increasing temperature from 297 K to 353 K, the critical corrosion currents of Ti electrodes in the mixture solution of 0.5 M H_2SO_4 and 0.59 mM NaF increased almost one order in magnitude. The buffer ability of the dealloying solutions also played an important role for the formation of nanoporous structures [22]. Since the HF solution had no buffer ability, the dissolution of Ti_2O and Ti atoms consumed hydrogen ions to generate hydrogen gas bubbles during dealloying [11]. As a result, the pH of the solution was increased. The formation of Cu_2O on $\text{Ti}_{60}\text{Cu}_{40}$ ribbon alloys was considered to be a direct evidence for the increase in pH. According to E–pH diagram of Cu in H_2O at 298 K, the critical pH for the formation of Cu_2O is higher than 6 [23]. When the pH of the solution was increased from 3 to 5, the critical corrosion current decreased more than one order of magnitude [24]. Therefore, the nanopores formed in $\text{Ti}_{60}\text{Cu}_{40}$ ribbons were relatively smaller than those of $\text{Ti}_{50}\text{Cu}_{50}$ ribbons.

From the physical perspectives, the diffusion and rearrangement of Cu adatoms are regarded to be the key steps for the formation of NPCs. These steps evoke mainly at the interfacial regions and these surface diffusion controlled processes exhibit a strong

Table 2

Activation energy and diffusion constant of dealloyed $\text{Ti}_{40}\text{Cu}_{60}$, $\text{Ti}_{50}\text{Cu}_{50}$ and $\text{Ti}_{60}\text{Cu}_{40}$ amorphous alloys derived from Eqs. (1) and (2).

Alloy system	Solutions (M HF)	Activation energy (E_a , kJ mol^{-1})	Diffusion constant (D_0 , $\text{m}^2 \text{ s}^{-1}$)
$\text{Ti}_{40}\text{Cu}_{60}$	0.03	78.1	8.45×10^{-6}
$\text{Ti}_{40}\text{Cu}_{60}$	0.13	77.9	7.14×10^{-4}
$\text{Ti}_{50}\text{Cu}_{50}$	0.03	55.3	3.00×10^{-7}
$\text{Ti}_{50}\text{Cu}_{50}$	0.13	67.9	2.03×10^{-6}
$\text{Ti}_{60}\text{Cu}_{40}$	0.03	40.3	7.60×10^{-12}
$\text{Ti}_{60}\text{Cu}_{40}$	0.13	74.1	2.42×10^{-4}

dependency on temperature [7]. Evangelakis et al. investigated the self-diffusion of Cu adatoms by the molecular dynamic method [25]. They found that Cu adatom diffusion took place exclusively by hopping from one adatom position to an adjacent one and that multiple jumps are frequent at low temperatures. Montalenti et al. found that the long jump occurred frequently at high temperatures [26]. The in-channel diffusion, such as single jump or double jump, is preferred at low temperatures. On the contrary, cross-channel jump diffusion, such as long jump or double exchange jump, may appear at high temperatures. When the temperature increased from 450 K to 600 K, the percentage of the long jump increased from 6% to 15% for Cu adatoms, and the single jumps were dominant at 450 K. Compared with Au, the long jumps are practically absent in the above mentioned temperature ranges, which is contributed to the formation of fine nanoporous structures for dealloyed Ag–Au alloys [7]. Boisvert et al. has reported that the frequency of jump is higher than that of exchange at the lower temperatures [27]. Therefore, in our experiments, the rough nanoporous structures formed at higher temperatures were mainly attributed to the increase in the cross-channel jump diffusion, which prevails in a longer diffusion distance and rearranges in relative larger length scales. Because the diffusion and rearrangement of Cu adatoms proceeded in a relative large scale length, the nanoporous structures had a large nanopores and wider ligaments at high temperatures. The formation of the narrow ligaments on Ti₆₀Cu₄₀ ribbon in 0.03 M HF solution at 348 K might be due to the complex effects of temperature and local pH changes.

4. Conclusion

In conclusion, an evolution of nanoporous structure from binary amorphous Ti_xCu_{100-x} ($x = 40, 50$ and 60 at.%) alloys was investigated from an aspect of Arrhenius relationships. An interpenetrating three-dimensional bi-continuous nanoporous structure of *fcc* Cu was formed at different temperatures with a pore size of 25–380 nm and a ligament size of 46–338 nm. The characteristic scale length of nanopores and ligaments at lower temperatures was almost one order of magnitude smaller than those formed at higher temperatures. The finer nanopores formed on Ti₄₀Cu₆₀ ribbons, which had a pore size of 25 nm in 0.03 M HF solution and 85 nm in 0.13 M HF solution are due to the high Cu content. The significant increases in the surface diffusivity from the dealloying temperatures accordingly formed the rougher nanostructures. The activation energy was estimated to be 40.3–78.1 kJ mol⁻¹, which depended on the alloy composites and concentrations of dealloying solutions. The long jump and cross-channel diffusion

are prevailed at higher temperatures, which resulted in the formation of rough nanoporous structure.

Acknowledgements

The authors gratefully acknowledge financial support by the Ministry of Education, Culture, Sports, Science, and Technology (MEXT) through Grant-In-Aid for Science Research in a Priority Area on “Research and Development Project on Advanced Materials Development and Integration of Novel Structured Metallic and Inorganic Materials” and a Grant-in-Aid for Young Scientists (B) under Grant No. 24760567. We would like to thank Mr. Kobayashi for his help with TEM observations.

References

- [1] D. Kramer, R.N. Viswanath, J. Weissmüller, *Nano Lett.* 4 (2004) 793–796.
- [2] G.C. Bond, D.T. Thompson, *Catal. Rev. Sci. Eng.* 41 (1999) 319–388.
- [3] T. You, O. Niwa, M. Tomita, S. Hirono, *Anal. Chem.* 75 (2003) 2080–2085.
- [4] J.R. Weissmueller, N. Viswanath, D. Kramer, P. Zimmer, R. Wuerschum, H. Gleiter, *Science* 300 (2003) 312–315.
- [5] Z.H. Zhang, Y. Wang, Z. Qi, W.H. Zhang, J.Y. Qin, J. Frenzel, *J. Phys. Chem., C* 113 (2009) 12629–12636.
- [6] J.S. Yu, Y. Ding, C.X. Xu, A. Inoue, T. Sakurai, M.W. Chen, *Chem. Mater.* 20 (2008) 4548–4550.
- [7] L.H. Qian, M.W. Chen, *Appl. Phys. Lett.* 91 (2007) 083105-1–083105-3.
- [8] Y. Ding, Y.J. Kim, J. Erlebacher, *Adv. Mater.* 16 (2004) 1897–1900.
- [9] J.R. Hayes, A.M. Hodge, J. Biener, A.V. Hamza, *J. Mater. Res.* 21 (2006) 2611–2616.
- [10] L.Y. Chen, T. Fujita, Y. Ding, M.W. Chen, *Adv. Funct. Mater.* 20 (2010) 2279–2285.
- [11] Z.H. Dan, F.X. Qin, Y. Sugawara, I. Muto, N. Hara, *Intermetallics* 29 (2012) 14–20.
- [12] D.R. Lide, *CRC Handbook of Chemistry and Physics*, 84th ed., CRC Press LLC, Boca Raton, London, New York, Washington, DC, 2003.
- [13] W. Klement, R.H. Jun, Willens, P. Duwez, *Nature* 187 (1960) 869–870.
- [14] A. Inoue, *Acta Mater.* 48 (2000) 263–279.
- [15] W.B. Liu, S.C. Zhang, N. Li, J.W. Zheng, Y.L. Xing, *Micropor. Mesopor. Mater.* 138 (2011) 1–7.
- [16] J. Erlebacher, M.J. Aziz, A. Karma, N. Dimitrov, K. Sieradzki, *Nature* 410 (2001) 450–453.
- [17] J. Erlebacher, *J. Electrochem. Soc.* 151 (2004) C614–C626.
- [18] A.L. Patterson, *Phys. Rev.* 56 (1939) 978–982.
- [19] J.M. Dona, J. Gonzalez-Velasco, *J. Phys. Chem.* 97 (1993) 4714–4719.
- [20] E.G. Seebauer, C.E. Allen, *Prog. Surf. Sci.* 49 (1995) 265–330.
- [21] M.J. Mandry, G. Rosenblatt, *J. Electrochem. Soc.* 119 (1972) 29–33.
- [22] Z.H. Dan, F.X. Qin, Y. Sugawara, I. Muto, N. Hara, *Intermetallics* 31 (2012) 157–164.
- [23] R.M. Garrels, C.L. Christ, *Solutions, Minerals and Equilibria*, Harper & Row, New York, 1965. pp. 216–222.
- [24] M. Nakasawa, S. Matsuya, T. Shiraishi, M. Ohta, *J. Dent. Res.* 78 (1999) 1568–1572.
- [25] G.E. Evangelakis, G.C. Kallinteris, N.I. Papanicolaou, *Surf. Sci.* 394 (1997) 185–191.
- [26] F. Montalenti, R. Ferrando, *Phys. Rev. B* 59 (1999) 5881–5891.
- [27] G. Boisvert, L.J. Lewis, *Phys. Rev. B* 56 (1997) 7643–7655.